

# Chapter 11

## Hybrid Rockets

### 11.1 Conventional bi-propellant systems

A liquid bi-propellant chemical rocket system is shown schematically in Figure 11.1. Oxidizer and fuel from separate tanks are pressure-fed or pump-fed into a combustion chamber where atomization, mixing, ignition and combustion takes place. Despite the apparent simplicity of the diagram, liquid rockets are extremely complex. The complexity comes from the fact that the chamber pressure is usually quite high and one or both of the propellants may be cryogenic. In addition, the liquids are usually fed into the combustion chamber at very high mass flow rates requiring high performance turbo-pumps usually powered by a small flow of the propellants through a separate burner and turbine. Many of the most spectacular rocket failures have involved liquid bi-propellant systems.

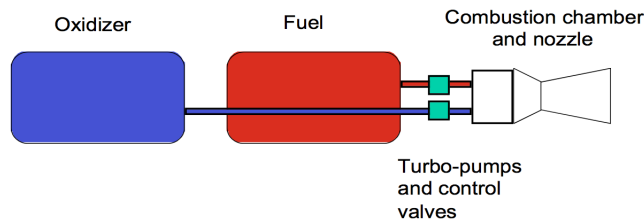


Figure 11.1: *Schematic of a liquid bi-propellant rocket system.*

Perhaps the most widely recognizable liquid engines are the space shuttle main engines that burn hydrogen and oxygen. These engines also make use of a pre-burner where most of the oxygen is burned with a small amount of hydrogen to raise the temperature of the gases that are injected into the main combustion chamber along with the rest of the hydrogen. The hydrogen is also used to regeneratively cool the rocket chamber and nozzle prior to mixing

with the oxygen. Many different oxidizers are used in bi-propellant systems. The two most popular are LOx (liquid oxygen) and  $N_2O_4$ . These are both very energetic oxidizers and burn readily with hydrocarbon fuels such as kerosene and alcohol as well as hydrazine ( $N_2H_4$ ). The ideal specific impulse of kerosene burning with LOx is approximately 360 seconds depending on the chamber pressure and nozzle area ratio.

Liquid rockets can be throttled by controlling the flow of fuel and oxidizer while keeping the ratio of oxidizer to fuel flow the same. Wide throttle ratios are somewhat difficult to achieve because of the reduced mixing that can occur at low liquid flow rates. Liquid rockets are subject to a variety of instabilities and the design and development of a new injector and combustion chamber is an expensive multi-year process.

Figure 11.2 depicts a solid rocket system. Though mechanically much simpler than liquids, the solid rocket is complicated by the use of an explosive mixture of fuel and oxidizer that involves a very complex and expensive manufacturing process. In addition solid rockets require stringent safety precautions in manufacture, handling and launch.

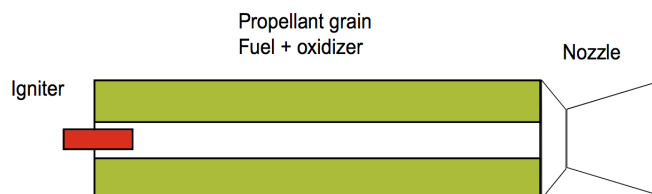


Figure 11.2: *Schematic of a solid rocket motor.*

The propellant regression rate for a solid rocket is proportional to the chamber pressure according to a relation of the form

$$\dot{r} = \alpha P_{t2}^n \quad (11.1)$$

where  $n < 1$ . Probably the most well known solids are the large re-usable space shuttle boosters. Each uses approximately a million pounds of propellant and produces roughly three million pounds of thrust at launch. The fuel is mainly aluminum in a polymer binder (Hydroxyl Terminated Poly-butadiene, HTPB) and the oxidizer is ammonium perchlorate (AP) which is the most widely used solid oxidizer. In general solid rockets use somewhat less energetic oxidizers than liquids and the specific impulse of solids is generally lower. The ideal specific impulse of the shuttle booster propellant is approximately 280 seconds depending on the nozzle area ratio. Recently ammonium perchlorate has been found in the groundwater near many of the rocket propellant processing plants across the US and concerns have been raised about the possible environmental impact of this chlorinated compound.

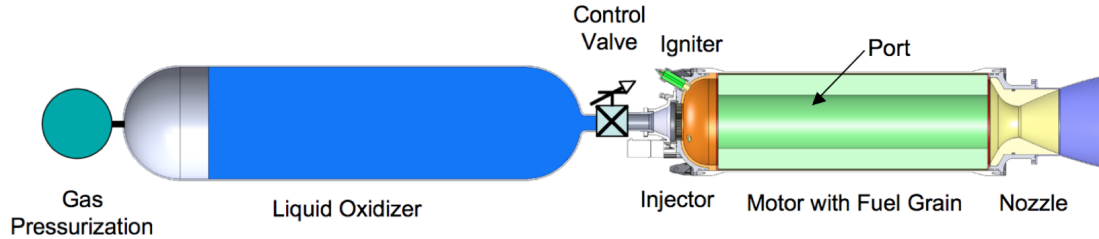
The hazardous operation of the two basic types of chemical rocket propulsion comes mainly from the oxidizer and fuel that must be mixed to release energy in the rocket combustion chamber. In liquid bi-propellant rockets, a pump leak or tank rupture that brings these chemicals together in an uncontrolled way can result in a large explosion. In solid propellant rockets, the fuel and oxidizer are pre-mixed and held together in a polymer binder. Cracks or imperfections in the propellant can cause uncontrolled combustion and explosion.

## 11.2 The hybrid rocket idea

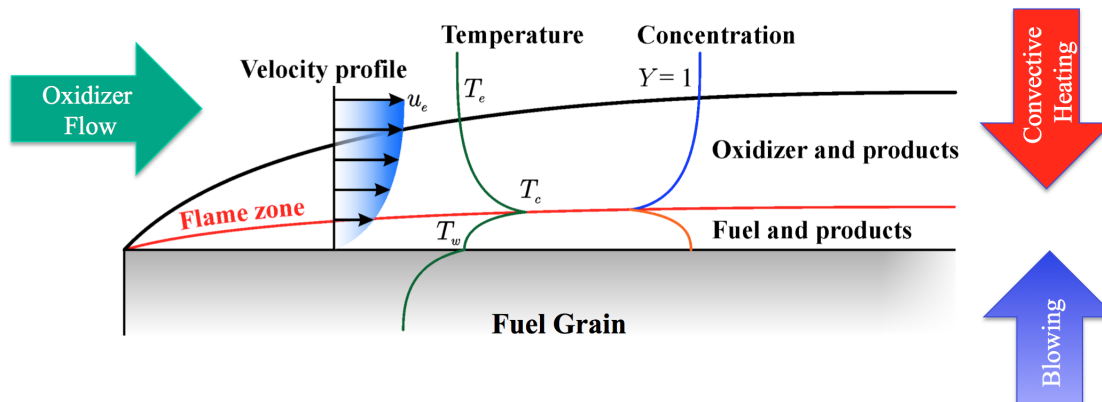
Figure 11.3 shows a hybrid rocket. The hybrid is inherently safer than other rocket designs. The idea is to store the oxidizer as a liquid and the fuel as a solid, producing a design that is less susceptible to chemical explosion than conventional solid and bi-propellant liquid designs. The fuel is contained within the rocket combustion chamber in the form of a cylinder with a circular channel called a port hollowed out along its axis. Upon ignition, a diffusion flame forms over the fuel surface along the length of the port. The combustion is sustained by heat transfer from the flame to the solid fuel causing continuous fuel vaporization until the oxidizer flow is turned off. In the event of a structural failure, oxidizer and fuel cannot mix intimately leading to a catastrophic explosion that might endanger personnel or destroy a launch pad.

The idea of the hybrid rocket has been known since the first flight in 1933 by Soviet researchers, but wasn't given serious attention until the 1960's. The primary motivation was the non-explosive character of the fuel, which led to safety in both operation and manufacture. The fuel could be fabricated at any conventional commercial site and even at the launch complex with no danger of explosion. Thus a large cost saving could be realized both in manufacture and launch operation. Additional advantages over the solid rocket are: greatly reduced sensitivity to cracks and de-bonds in the propellant, better specific impulse, throttle-ability to optimize the trajectory during atmospheric launch and orbit injection and the ability to thrust terminate on demand. The products of combustion are environmentally benign unlike conventional solids that produce acid forming gases such as hydrogen chloride.

The hybrid rocket requires one rather than two liquid containment and delivery systems. The complexity is further reduced by omission of a regenerative cooling system for both the chamber and nozzle. Throttling control in a hybrid is simpler because it alleviates the requirement to match the momenta of the dual propellant streams during the mixing process. Throttle ratios up to 10 have been common in hybrid motors. The fact that the fuel is in the solid phase makes it very easy to add performance enhancing materials to the fuel such as aluminum powder. In principle, this could enable the hybrid to gain an  $I_{sp}$  advantage over a comparable hydrocarbon fueled liquid system.

Figure 11.3: *Schematic of a hybrid rocket motor.*

Boundary layer combustion is the primary mechanism of hot gas generation in hybrid rockets. The idealized sketch in Figure 11.4 illustrates the flow configuration. The hybrid normally uses a liquid oxidizer that burns with a solid fuel although reverse hybrids such as liquid hydrogen burning with solid oxygen have been studied. The flame thickness and location in the boundary layer are shown roughly to scale. The flame zone is relatively deep in the boundary layer and the flame tends to be fuel rich based on the observed flame position and relatively low flame temperatures measured in the boundary layer. The hybrid enjoys many safety and environmental advantages over conventional systems, however large hybrids have not been commercially successful. The reason is that traditional systems use polymeric fuels that evaporate too slowly making it difficult to produce the high thrust needed for most applications.

Figure 11.4: *Boundary layer combustion.*

### 11.2.1 The fuel regression rate law

Theory shows that the fuel mass transfer rate is proportional to the mass flux averaged

across the port. The mass flow rate increases with axial distance along the port leading to coupling between the local fuel regression rate and the local mass flux. For proper design, accurate expressions are needed for both the time dependent oxidizer-to-fuel ratio at the end of the port, and the time at which all the fuel is consumed. As the fuel is depleted the flame approaches the motor case at which point the burn must be terminated. The coupling between the local regression rate and the local mass flow rate means that both variables depend on time and space. This complicates the analysis of the thrust time behavior of the hybrid compared to a solid rocket. The problem is governed by two coupled first-order partial differential equations, the regression rate equation

$$\frac{\partial r(x, t)}{\partial t} = \frac{a}{x^m} \left( \frac{\dot{m}_{port}}{\pi r^2} \right)^n \quad (11.2)$$

and the mass flow growth equation

$$\frac{\partial \dot{m}_{port}(x, t)}{\partial x} = \rho_f (2\pi r) \frac{a}{x^m} \left( \frac{\dot{m}_{port}}{\pi r^2} \right)^n. \quad (11.3)$$

The local mass flux in the port is generally denoted  $G$  where

$$G = \frac{\dot{m}_{port}}{\pi r^2} = \frac{\dot{m}_{ox} + \dot{m}_f}{\pi r^2}. \quad (11.4)$$

The local port mass flow rate,  $\dot{m}_{port}$ , is the sum of the oxidizer mass flow rate,  $\dot{m}_{ox}$ , injected at the entrance to the port and the accumulated fuel mass flow rate,  $\dot{m}_f$ , transferred from the fuel grain upstream of a location  $x$ . The coefficient  $a$  is an empirical constant determined by the choice of fuel and oxidizer. The units of the regression rate constant are

$$[a] = \frac{Length^{2n+m+1}}{Mass^n Time^{1-n}}. \quad (11.5)$$

The dependence of regression rate on mass flux  $G$  and stream-wise coordinate  $x$  arises from the dependence of the skin friction and heat transfer rate on Reynolds number based on distance along the port. Values of the exponents suggested by theory are  $m = 0.2$  and  $n = 0.8$ . Measured values of  $n$  tend to be in the range 0.3 to 0.8 depending on the choice of fuel and oxidizer. Values of  $n$  greater than 0.8 or less than about 0.3 are generally not observed. The length exponent turns out to be very difficult to measure since it is relatively small and would require a large number of motor tests at a wide range of scales to be determined accurately. As nearly as one can tell at this point  $m$  is considerably smaller than the prediction of classical theory.

A widely used approximation to (11.2) and (11.3) is the single equation

$$\frac{dr}{dt} = a_o G_{ox}^m. \quad (11.6)$$

where the port length effect is neglected and the fuel regression rate is assumed to only depend on the oxidizer mass flux, which is constant along the port. In general, equation (11.6) underestimates the fuel mass generation rate. However, (11.6) can be a reasonably accurate approximation in situations where the design  $O/F$  ratio is relatively large, more than 5 or so.

A greater problem is that the vast majority of values of the regression rate constant reported in the literature correspond to  $a_o$  based on data measured against (11.6). The problem with this is that every change in the value of  $O/F$  for a given test motor requires the determination of a new value of  $a_o$ . In point of fact the  $O/F$  generally varies during the course of a burn and so the reported value of  $a_o$  also depends on how the mean  $O/F$  is determined. Consider

$$\begin{aligned} \frac{\partial r(x, t)}{\partial t} &= \frac{a}{x^m} \left( \frac{\dot{m}_{port}}{\pi r^2} \right)^n = \\ &= \frac{a}{x^m} \left( \frac{\dot{m}_{ox} (1 + 1/(\dot{m}_{ox}/\dot{m}_f(x, t)))}{\pi r^2} \right)^n = \frac{a(1 + 1/(OF(x, t)))^n}{x^m} \left( \frac{\dot{m}_{ox}}{\pi r^2} \right)^n. \end{aligned} \quad (11.7)$$

If the basic regression rate equations (11.3) and (11.4) are to be believed then

$$a_o = a(1 + 1/(OF(x, t)))^n. \quad (11.8)$$

In principle  $a_o$  is a function of space and time. It can only be treated as a constant if some scheme of space time averaging of the  $O/F$  ratio is used for a given run and, even then,  $a_o$  will have a new value every time the  $O/F$  is changed. Unfortunately, when  $a_o$  is reported in the literature, the corresponding  $O/F$  is often not reported. A consequence is that today we often do not have good, solid empirical values of the regression rate constants for many propellant combinations.

In marked contrast to solid rockets, the regression rate of a hybrid is insensitive to the chamber pressure except at very low fluxes where radiation effects become important and at very high fluxes where chemical kinetics effects are important. This important characteristic enables the chamber pressure to be a free variable in the motor design enabling the designer to optimize the chamber pressure for a given mission. Although the hybrid seems to lie somewhere between a liquid and a solid system it has advantages that are unique and not enjoyed by liquids or solids.

### 11.2.2 Specific impulse

The theoretical specific impulse of a hybrid rocket is more appropriately compared to a bi-propellant liquid than a solid. The oxidizer can be any of the oxidizers used with liquid bi-propellant engines. Typically, the solid fuel is a polymeric hydrocarbon such as hydroxyl-terminated-poly-butadiene (HTPB), a common solid propellant binder with an energy density comparable to kerosene. But, hybrid solid fuel mass densities are typically 15-20 % greater than the density of liquid kerosene. Figure 11.5 (left) depicts the theoretical specific impulse versus oxidizer to fuel  $O/F$  ratio of liquid oxygen (LOx) burning with paraffin and HTPB. A plot of LOx burning with liquid kerosene would look very similar.

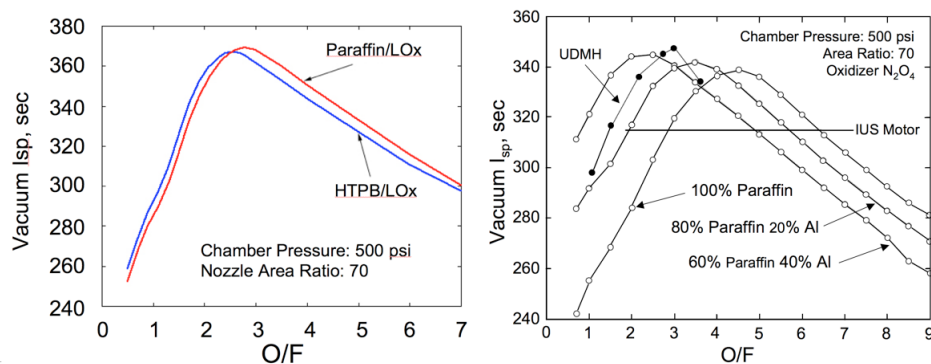


Figure 11.5: *Left figure, ideal specific impulse for paraffin and HTPB burning with LOx. Right figure paraffin-aluminum mixtures burning with nitrogen tetroxide. The IUS (Inertial Upper Stage) motor was a solid rocket built by the Chemical Systems Division of United Technologies and used as an upper stage in Boeing satellite launches for many years.*

The plot on the right of Figure 11.5 shows the specific impulse of paraffin burning with  $N_2O_4$  with varying percentages of aluminum added to the fuel by mass. Aluminum addition tends to increase the specific impulse slightly while reducing the optimal  $O/F$  allowing the designer to use a smaller liquid storage and feed system. These figures give a pretty good illustration of the range of  $O/F$  ratios used in typical systems. Generally, the oxidizer mass flow rate tends to be two or more times the fuel mass flow rate at the end of the port.

### 11.2.3 The problem of low regression rate

The main drawback of the hybrid is that the combustion process relies on a relatively slow mechanism of fuel melting, evaporation and diffusive mixing as depicted in Figure 11.4. In a solid rocket, the flame is much closer to the fuel surface and the regression rate is typically an order of magnitude larger. As a rough comparison, the regression rate in a solid rocket

at a typical rocket combustion chamber pressure may be on the order of  $1.0\text{ cm/sec}$  whereas a typical hybrid using a classical polymeric fuel such as HTPB may have a regression rate on the order of  $0.1\text{ cm/sec}$ . To compensate for the low regression rate, the surface area for burning must be increased. This is accomplished through the use of a multi-port fuel grain such as that depicted in Figure 11.6. Most attempts to increase the regression rate involve some method for increasing the heat transfer rate to the fuel surface. This can be done, for example, by increasing turbulence levels in the port or by adding roughness to the fuel grain. The problem is that as the heat transfer rate is increased, the radial velocity of the evaporating fuel toward the center of the port increases. This so-called "blocking effect" tends to decrease the temperature gradient at the fuel surface leading to a reduction in the amount of heat transfer increase that can be achieved. A regression rate increase on the order of 25-30 % or so can be obtained using this approach - not the factor of 2 or 3 that is needed for a single port design.

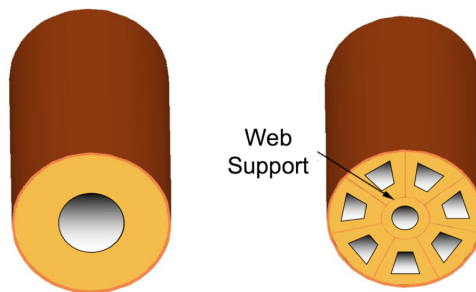


Figure 11.6: *Single versus multi-port (wagon wheel) grain design.*

The most obvious problem with the multi-port design is that the amount of fuel that can be loaded into a given volume is reduced, leading to an increase in the vehicle diameter for a given total fuel mass. There are other problems. The grain may need to be produced in segments and each segment must be supported structurally, adding weight and complexity. In addition it is very difficult to get each port to burn at the same rate. If one burns slightly faster than another, then the oxidizer will tend to follow the path of least resistance leading to further disparity in the oxidizer flow rate variation from port to port. Toward the end of burning, the port that reaches the liner first forces the motor to be shut down prematurely leading to an inordinately large sliver fraction of unburned fuel. Small pressure differences from port to port can lead to grain structural failure and loss of fuel fragments through the nozzle. Aside from possible damage to the nozzle, the resulting increase in the overall  $O/F$  ratio leads to a reduction of the specific impulse and an increase in the nozzle throat erosion rate. Due to the high erosion, the nozzle area ratio decreases excessively leading to an additional loss of specific impulse.

### 11.3 Historical perspective

Early hybrid rocket development and flight test programs were initiated both in Europe and the U.S. in the 1960's. The European programs in France and Sweden involved small sounding rockets, whereas the American flight programs were target drones (Sandpiper, HAST, and Firebolt) which required supersonic flight in the upper atmosphere for up to 5 minutes. These latter applications were suitable for the conventional hybrid because its very low burning rate was ideal for a long duration sustainer operation.

Despite the very low regression rate of the fuel, in the late 1960's Chemical Systems Division of United Technologies (CSD/UTC) investigated motor designs of larger diameters that could produce high thrust suitable for space launch vehicles. They experimented with a 38 *inch* diameter motor delivering 40,000 *lbs* of thrust. In order to achieve a high mass flow rate, a motor with 12 ports in the fuel grain was required. Although the motor was successfully fired several times, it was recognized that the poor volumetric fuel loading efficiency would lead to a deficit in vehicle performance.

Interest in the hybrid was revived again in the late 1970's when concern was expressed for the storage and handling of the large solid propellant segments of the Shuttle booster. The storage of potentially explosive grains is costly in terms of requirements for reinforced structures and interline distance separation. The same safety concern arose again after the Space Shuttle Challenger disaster, where it was recognized that a thrust termination option might have avoided the failure. This concern was heightened when, a few months later, there was a Titan failure, caused by an explosion of one of the solid boosters.

Several hybrid propulsion programs were initiated in the late 80's and early 90's. The Joint Government/Industry Research and Development (JIRAD) program involved the testing of 11 and 24 *inch* diameter hybrid motors at the Marshall Space Flight Center. Another hybrid program initiated during the early 90s was DARPA's Hybrid Technology Options Project (HyTOP). The goal of this program was to develop the HyFlyer launch vehicle and demonstrate the feasibility of hybrid boosters for space applications. The members of the HyTOP team were AMROC, Martin Marietta and CSD/UTC.

In the 1990s, two significant hybrid efforts occurred. One was the formation of the American Rocket Company (AMROC), an entrepreneurial industrial company devoted entirely to the development of large hybrid boosters. The second, with encouragement from NASA, was the formation of the Hybrid Propulsion Industry Action Group (HPIAG) composed of both system and propulsion companies devoted to exploring the possible use of hybrids for the Shuttle booster and other launch booster applications. Both efforts ran into technical stumbling blocks, basically caused by the low regression rate fuels, which resulted in large diameter motors with many ports to satisfy thrust requirements. The resulting configuration not only compromised potential retrofit for the Shuttle and Titan boosters

but also raised questions about the internal ballistic performance of a thin web multi-port motor, especially toward the end of burning when the web approaches structural failure. Although AMROC had many successful tests in 51 inch diameter motors, they ran into difficulties when the motor was scaled to 6 foot diameter and 250,000 pounds of thrust. The low regression rate of the fuel dictated a 15 port grain design and problems of poor grain integrity were the result. In 1995 AMROC filed for bankruptcy.

The Hybrid Propulsion Demonstration Program (HPDP) began in March 1995. The goal of the HPDP was to enhance and demonstrate several critical technologies that are essential for the full scale development of hybrid rocket boosters for space launch applications. The government and industry participants in the program were NASA, DARPA, Lockheed Martin, CSD/UTC, Thiokol, Rocketdyne, Allied Signal and Environmental Aerospace Corporation. Even though the tasks of the HPDP program included systems studies and sub-scale testing, the main objective of the program was the design and fabrication of a 250,000 pound thrust test-bed. The design of the motor was guided by the sub-scale motor tests performed under the JIRAD program. The wagon wheel 7+1 multi-port fuel grain was made of conventional hydroxyl-terminated-polybutadiene (HTPB)/ Escorez fuel. The motor was fired for short times in July 1999. The motor exhibited large pressure oscillations and unequal burning rates in the various ports. Later the motor was stabilized by substantially increasing the heat input at the fore end of the motor. Problems related to low regression rate inherent in conventional hybrids fuels were not solved.

The most recent advance in hybrid rockets occurred in the Fall of 2004 when SpaceShipOne carried a pilot to over 328,000 feet to win the Ansari X-prize. This privately funded, sub-orbital flight seemed to usher in a new era in space tourism although the follow-on SpaceShipTwo has experienced lengthy delays in development.



Figure 11.7: *Space Ship One carried aloft by the White Knight carrier aircraft.*

The propulsion system for Space Ship One used a four port motor fueled by HTPB with nitrous oxide ( $N_2O$ ) as the oxidizer. Although the flight of Space Ship One was a great success, it was not exactly a walk in the park for the pilot. The description in Figure 11.9



Figure 11.8: *Various systems of Space Ship One. Note the hybrid rocket on the left.*

reveals a pretty sobering picture of the flight.

Neither SpaceDev or eAc met Scaled's wishes. The SpaceDev design, which has four longitudinal ports in the rubber fuel for enough burning area for high thrust, comes on with a bang, producing maximum thrust at the start—not the smooth ramp-up envisioned to turn the corner. The peak thrust is only about 85% of the desired plateau, and declines steadily from there, according to the Sept. 18 SETP presentation. Despite the early start, this still means that to get enough total impulse to loft SpaceShipOne above 100 km., the motor has to run longer than desired, in the very thin atmosphere where control is tenuous.

The webs of rubber between the four SpaceDev ports thin out and come apart toward the end of the run. The chunks extrude through the nozzle, causing frightening shaking and explosion noises in the cockpit. It happened at least three times on one flight and Melvill thought the tail had blown off. After minutes by himself in zero-g and entry, he was relieved when chase aircraft said the spaceship appeared alright.

The eAc motor didn't ignite until five sec. after the switch was thrown, and then also came on with a bang, but the initial combustion instabilities were less. It has a single port and compensates for the lower burning area with fuel additives to increase burning rate. But not enough, because it only made about 65% of the desired thrust. That required the burn time to be even longer for sufficient total impulse, extending the engine run farther out of the atmosphere.

Longer burn time of the eAc motor was considered the more serious problem, and the contract went to SpaceDev.

Mike Dornheim - Aviation Week  
October 18, 2004 page 36

Figure 11.9: *Space Ship One hybrid motor operation as described in Aviation Week.*

The conclusion from this history is that if a significantly higher burning rate fuel can be developed for the hybrid motor, the multi-port difficulties just described can be alleviated and a smaller, safer more efficient motor can be designed. Although this deficiency of conventional hybrid fuels was recognized more than forty years ago, attempts to increase the burning rate by more than 50-100 %, without compromising the safety and low-cost features of the hybrid design, have been largely unsuccessful until recently.

## 11.4 High regression rate fuels

In the late 1990s, the U.S. Air Force studied some exotic cryogenic designs for hybrid rockets. One scheme would have swapped the roles of the fuel and oxidizer. The fuel was liquid hydrogen and the oxidizer was solid oxygen. While investigating this unusual configuration, the Air Force also studied a different combination of cryogenic propellants: liquid oxygen and pentane, a hydrocarbon that is liquid at room temperature, but in this application was frozen solid using a bath of liquid nitrogen. The Air Force researchers found that solid pentane burns 3 to 4 times faster than normal fuels. The Air Force researchers kindly shared their data with us and after some careful analysis it appeared that mass transfer from the surface of this fuel involved more than simple evaporation.

Pentane produces a very thin, low viscosity, low surface tension, liquid layer on the fuel surface when it burns. The instability of this layer driven by the shearing effect of the oxidizer gas flow in the port leads to the lift-off and entrainment of droplets into the gas stream greatly increasing the overall fuel mass transfer rate. The multitude of entrained droplets offers an enormous amount of surface area for evaporation and burning without the usual reduction caused by the blocking effect. The basic mechanism is sketched in Figure 11.10.

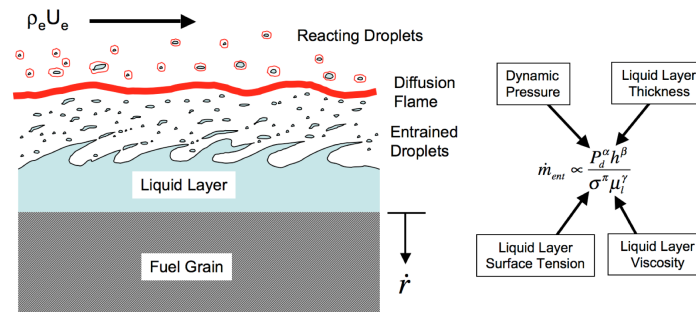


Figure 11.10: *Liquid layer entrainment mechanism.*

In effect, this mechanism acts like a continuous spray injection system distributed along the port with most of the fuel vaporization occurring around droplets convecting between the melt layer and the flame front. Since droplet entrainment is not limited by diffusive heat transfer to the fuel from the combustion zone, this mechanism can lead to much higher surface regression rates than can be achieved with conventional polymeric fuels that rely solely on evaporation. Equation (11.9) shows how the entrainment mass transfer component of the regression rate illustrated in Figure 11.10 depends on the parameters of the flow: the chamber pressure,  $P$ , liquid layer thickness,  $h$ , surface tension,  $\sigma$  and viscosity,  $\mu$ . The exponents in (11.9) are determined empirically and are of order one.

$$\dot{m}_{\text{entrainment}} \sim \frac{P_d^\alpha h^\beta}{\sigma^\pi \mu_l^\gamma} \quad (11.9)$$

The key fuel properties are in the denominator of (11.9) - low surface tension and low viscosity of the melt layer, evaluated at the characteristic temperature of the layer. This forms the basis of a fundamental criterion that can be used to identify high regression rate fuels. Not all fuels that form a melt layer at the fuel surface will entrain. For example, high-density-polyethelene (HDPE), which is a conventional hybrid fuel, does form a melt layer but the viscosity of the liquid is four orders of magnitude larger than pentane - too viscous to permit significant droplet entrainment. But frozen pentane itself is not a particularly promising fuel. It is not practical to have to soak the rocket motor in a liquid nitrogen bath before launch. This led to a search for a fuel that would be solid at room temperature, that would produce a low-viscosity liquid when it melted, and would be strong enough to withstand the high-temperature, high-pressure, high-vibration environment of a rocket motor's combustion chamber. To achieve this goal it was necessary to solve a puzzle.

Figure 11.11 shows the effect of molecular weight on the melt temperature and boiling temperature for the normal alkanes. The middle curve is an estimate of the mean melt layer temperature. The normal alkanes are linear, fully saturated hydrocarbons with the formula  $C_n H_{2n+2}$ . Familiar examples include methane (one carbon atom per molecule), ethane (two carbons), and propane (three carbons). As the number of carbon atoms in the molecule increases, the normal alkanes become room-temperature liquids, such as pentane (five carbons), and eventually solids such as waxes and polyethelene.

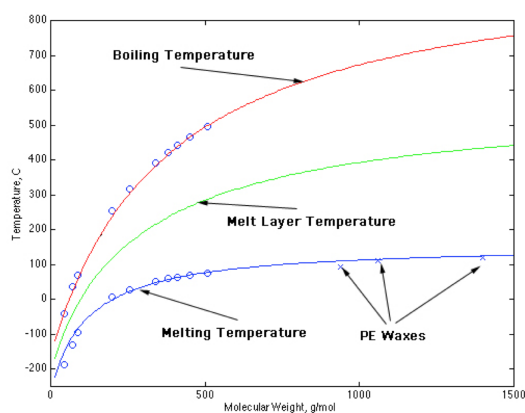


Figure 11.11: *Effect of molecular weight on key temperatures for the normal alkanes.*

The crucial point of Figure 11.11 is this. The melt layer temperature rises quickly at low molecular weights but much more slowly at high molecular weights. In general, the viscosity of a liquid tends to increase with molecular weight. But, the viscosity of most liquids tends

to decrease exponentially fast with temperature. These facts can be applied to the melt layer of the normal alkanes. At high molecular weight, where the melt layer temperature increases only slowly, the viscosity increases through the dominance of the molecular weight effect. But at lower molecular weight, where the melt layer temperature increases rapidly, the tendency for the viscosity to increase with molecular weight is strongly offset by the tendency for viscosity to decrease with temperature.

The design goal is to find a hydrocarbon with the right molecular weight. At high molecular weights, the viscosity of the liquid form of the alkane is too large for droplets to form readily. At low molecular weights, the alkanes are either gaseous or liquid or soft solids, much too weak to withstand the rigors of a rocket combustion chamber. In between is a sweet spot; Fuels with roughly 25 to 50 carbon atoms per molecule that are structurally robust and produce low-viscosity liquids when they melt. Figure 11.12 indicates schematically the range of carbon numbers that are likely to produce significant entrainment mass transfer.

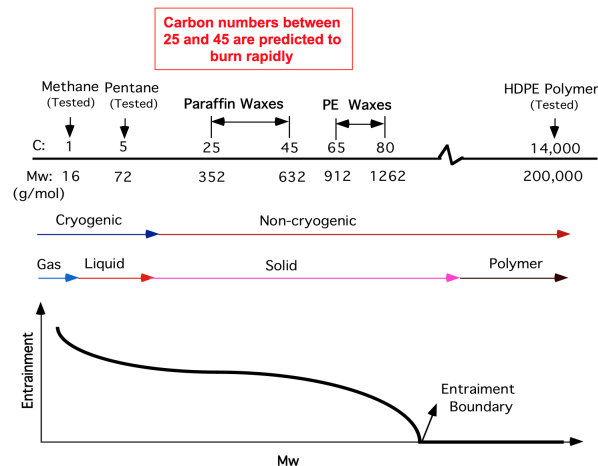


Figure 11.12: Schematic diagram indicating the normal alkanes that are expected to exhibit high regression rate.

These fuels, which include the paraffin waxes and polyethylene waxes, are predicted to have high regression rates at oxidizer mass fluxes covering a wide range of hybrid rocket applications. In fact, the viscosity of the melt layer in paraffin is comparable to pentane and so the regression rate is also similar despite the disparity in molecular weight. The kind of paraffin wax we use is a relatively high carbon number, fully refined, wax sometimes called sculptor's wax or hurricane wax. Fabricating, handling, and transporting traditional solid-rocket propellants is usually very costly, but a paraffin-based fuel is easy to deal with in all those regards. It is nontoxic, and indeed not hazardous at all. What's more, the complete combustion of this fuel with oxygen produces no hazardous gases. The products are simply

carbon dioxide and water. In contrast, the by-products of burning conventional solid rocket propellant often include carbon monoxide as well as acid forming gases such as hydrogen chloride. A more benign, easier to use, rocket fuel could hardly be imagined!

Regression rates 3 to 4 times the predicted classical rate have been observed in a laboratory scale motor using gaseous oxygen and an industrial grade paraffin wax. The specific impulse of a paraffin-based hybrid motor is slightly higher than that of a kerosene-based liquid motor and solid paraffin is approximately 20% more dense than liquid kerosene. Figure 11.4 shows the ideal specific impulse of paraffin wax and HTPB burning with liquid oxygen. The waxes comprise a wide range of molecular weight, surface tension and viscosity and therefore can be used to create mixtures whose regression rate characteristics are tailored for a given mission.

## 11.5 The $O/F$ shift

Over the course of a burn at a fixed oxidizer mass flow rate there is a tendency for the oxidizer to fuel ( $O/F$ ) ratio to shift to higher values as the port opens up. This can be seen from the following. For a single circular port a rough estimate of the  $O/F$  ratio at the end of the port is, using (11.6)

$$O/F = \frac{\dot{m}_o}{\dot{m}_f} = \frac{\dot{m}_o}{\rho_f \pi D L \alpha \left(\frac{\dot{m}_o}{\pi r^2}\right)^n} = \frac{\dot{m}_o^{1-n} D^{2n-1}}{4^n \pi^{1-n} \alpha \rho_f L} \quad (11.10)$$

where  $L$  is the port length and  $r$  is the port radius. Recall that the exponent is generally in the range  $0.6 < n < 0.8$ . As the port diameter increases the burning area increases and the oxidizer mass flux goes down. For  $n > 0.5$  the decrease in mass flux dominates the increase in burning area and the overall generation rate of fuel mass goes down. The net effect is to cause the chamber pressure and hence the thrust to decrease naturally over the course of the burn as the vehicle mass decreases. This feature is desirable for a launch system where the payload is subject to a maximum acceleration constraint. Compare this to a solid rocket where the thrust tends to increase during the burn and a throttling option is not available.

Note the relatively strong sensitivity in Figure 11.4 of the specific impulse to the  $O/F$  ratio. The change of  $O/F$  implies a change in specific impulse and a possible reduction in vehicle performance. This is a factor that must be taken into account by the designer seeking to get maximum total delivered impulse from the motor. In practice the maximum payload acceleration limit leads to a requirement that the oxidizer mass flow be throttled back while the port opens up and the two effects tend to offset one another. A typical case might be a factor of two decrease in the oxidizer mass flow rate and a factor of three

increase in the port diameter. For  $n = 0.62$  the net effect is less than a one percent change in  $O/F$ .

## 11.6 Scale-up tests

To demonstrate the feasibility of high regression rate fuels, a series of tests were carried out on intermediate scale motors at pressures and mass fluxes representative of commercial applications. A hybrid test facility designed to study these fuels was developed by NASA and Stanford researchers at NASA Ames Research Center. An image from one of these tests is shown in Figure 11.13.

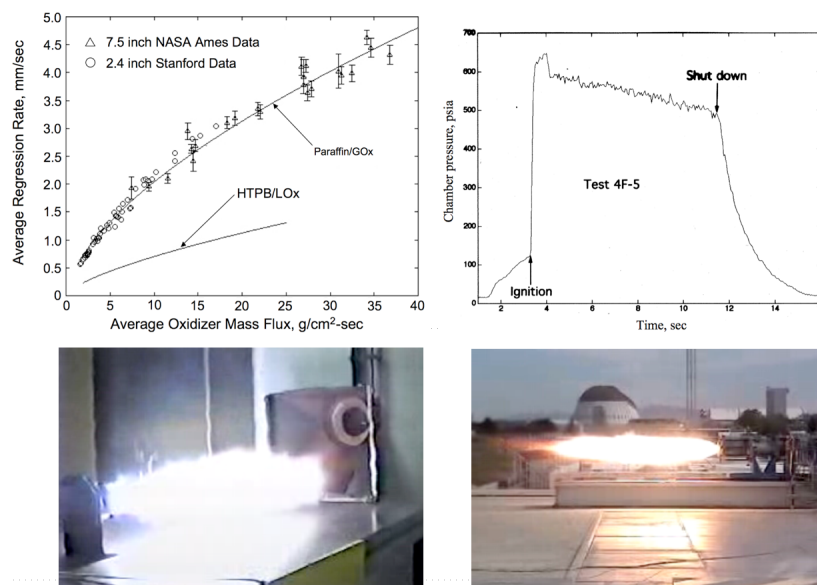


Figure 11.13: *Hybrid motor tests at Stanford and NASA Ames showing a typical pressure time history of the Ames tests. Thrust in the image shown is approximately 10000 Newtons with a simple convergent nozzle.*

Figure 11.14 shows the main results of these tests as well as earlier results of testing on a laboratory scale motor at Stanford. The results are compared with HTPB.

The main conclusions from these tests are the following.

- 1) The regression rate behavior observed in the small scale tests at Stanford prevails when the motor is scaled up to chamber pressures and mass fluxes characteristic of operational systems. Moreover the regression rate data from large and small motors matches quite well indicating that small scale tests can be used to infer the behavior of larger motors.

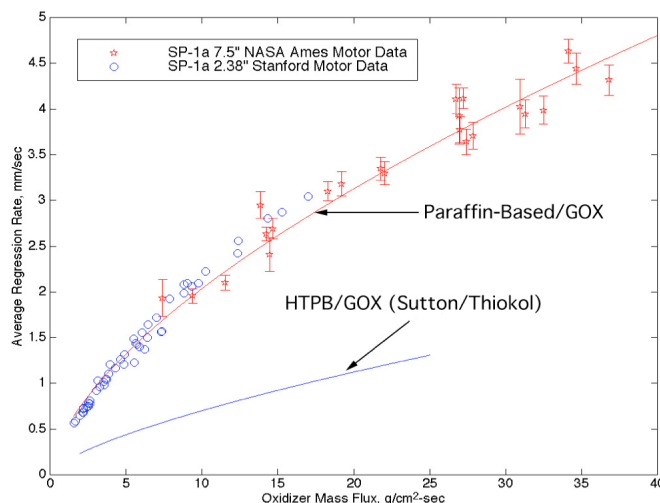


Figure 11.14: Regression rate versus oxidizer mass flux for paraffin and HTPB.

This is extremely useful when it comes to developing the right fuel formulation for a given mission.

- 2) Paraffin-based fuels provide reliable ignition and stable combustion over the entire range of mass fluxes encountered ( $50 - 600 \text{ kg/m}^2 - \text{sec}$ ).
- 3) The fuel exhibited excellent structural integrity over the range of chamber pressures used ( $10 - 65 \text{ bar}$ ).

## 11.7 Regression rate analysis

### 11.7.1 Regression rate with the effect of fuel mass flow neglected.

The simplest approach to determining how the port radius varies with time is to neglect the effect of accumulated fuel mass flow on the regression rate and assume the length exponent  $m = 0$  so the port radius is independent of  $x$ . This utilizes the fact that  $m$  is known to be small allowing the singularity at  $x = 0$  to be removed. Moreover the optimal  $O/F$  is often three or more so the oxidizer usually comprises most of the mass flow. Recall (11.6) and express the mass flux in terms of the radius and oxidizer mass flow.

$$\frac{dr(t)}{dt} = a_o \left( \frac{\dot{m}_{ox}(t)}{\pi r^2} \right)^n \quad (11.11)$$

Integrate (11.11) with respect to time.

$$r(t) = \left( r(0)^{2n+1} + (2n+1) \frac{a_o}{\pi^n} \int_0^t \dot{m}_{ox}(t')^n dt' \right)^{\frac{1}{2n+1}} \quad (11.12)$$

Under the assumed regression rate (11.11) law the mass flow increases linearly along the port.

$$\frac{\dot{m}_{port}}{\dot{m}_{ox}} = \frac{\dot{m}_f + \dot{m}_{ox}}{\dot{m}_{ox}} = 1 + \left( \frac{2\pi^{1-n} a_o \rho_f}{\dot{m}_{ox}^{1-n} \left( r(0)^{2n+1} + (2n+1) \frac{a_{ox}}{\pi^n} \int_0^t \dot{m}_{ox}(t')^n dt' \right)^{\frac{2n-1}{2n+1}}} \right) x \quad (11.13)$$

### 11.7.2 Exact solution of the coupled space-time problem for $n = 1/2$ .

In reality the regression rate is dependent on the local total mass flux including the fuel mass accumulated along the port and, in turn, the local mass flux depends on the local radius. The problem is governed by two coupled first-order partial differential equations, (11.2) and (11.3). For  $n = 1/2$  the equations simplify to

$$\frac{\partial}{\partial t} (r^2) = 2\pi^{-1/2} a \frac{\dot{m}_{port}^{1/2}}{x^m} \quad (11.14)$$

and

$$\frac{\partial \dot{m}_{port}}{\partial x} = 2\pi^{1/2} a \rho_f \frac{\dot{m}_{port}^{1/2}}{x^m} \quad (11.15)$$

The solution of (11.14) and (11.15) is

$$r(x, t) = \left( r(x, 0)^2 + \frac{2a}{x^m \pi^{1/2}} \left( \int_0^t \dot{m}_{ox}(t')^{1/2} dt' + \frac{\pi^{1/2} a \rho_f x^{1-m} t}{1-m} \right) \right)^{1/2} \quad (11.16)$$

and

$$\dot{m}_{port}(x, t) = \left( \dot{m}_{ox}(t)^{1/2} + \frac{\pi^{1/2} a \rho_f x^{1-m}}{1-m} \right)^2 \quad (11.17)$$

For  $n = 1/2$ , the increased fuel mass generation due to the increase in port surface area is exactly compensated by the decrease in mass flux due to the growth in port cross-sectional area. As a result the total mass flow rate (11.17) at any point in the port is independent of time if  $\dot{m}_{ox}$  is constant. For  $n > 1/2$  the effect of decreasing mass flux dominates the increase in port surface area and the mass flow rate at a given coordinate along the port  $x$  decreases with time as the port opens up. If  $n < 1/2$  the mass flow rate increases with time. Note that according to (11.16), shortly after the oxidizer flow is initiated the radius of the fore end of the port is infinite if the length exponent,  $m > 0$ . Figure 11.15 shows a typical shape of the port after some period of time has elapsed after ignition. There is typically a minimum radius point near the fore end of the port downstream of which the port opens up slightly.

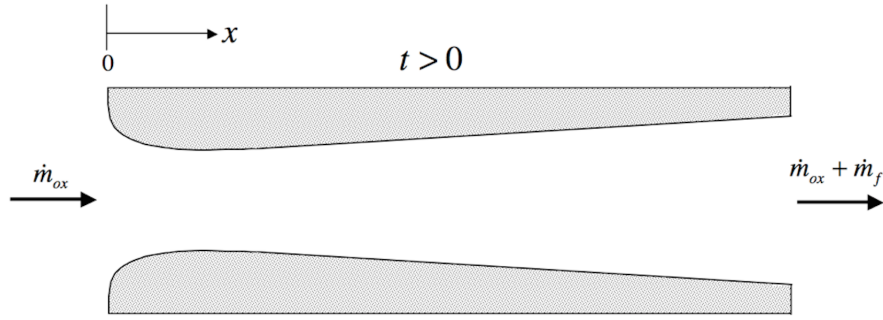


Figure 11.15: Typical port shape at the end of a burn for  $m > 0$ .

### 11.7.3 Similarity solution of the coupled space-time problem for general $n$ and $m$ .

For general values of  $n$  and  $m$  the coupled equations (11.2) and (11.3) can be solved numerically given the initial port geometry and oxidizer mass flow rate,  $\dot{m}_{ox}(t)$ . Reference [1] discusses the coupled problem and includes an example of a numerical solution. As it turns out, (11.2) and (11.3) admit a similarity solution for constant  $\dot{m}_{ox}$ . This allows the equations to be reduced to a pair of ODEs in the similarity variable

$$\theta = \left( \frac{(\pi^{-n}a)^2 (2\pi\rho_f)^{(2n+1)}}{\dot{m}_{ox}} \right)^{\frac{1}{2n-2m+1}} \frac{x}{t^{\left(\frac{2n-1}{2n-2m+1}\right)}}. \quad (11.18)$$

The similarity solution is derived in reference [2]. It can be used to generate accurate solutions for the port radius and  $O/F$  ratio. The similarity solution can even be applied

to the case where  $\dot{m}_{ox}$  does change with time by using a staircase function to approximate  $\dot{m}_{ox}$ .

#### 11.7.4 Numerical solution for the coupled space-time problem, for general $n$ and $m$ and variable oxidizer flow rate.

The coupled equations (11.2) and (11.3) can be solved for a general initial port radius distribution and variable oxidizer mass flow rate using a first order forward difference scheme. First, the equations are non-dimensionalized using the initial oxidizer mass flow rate,  $\dot{m}_{ox}(0)$ , the initial port radius at the fore end,  $r(0,0)$  and the burn time,  $t_{burntime}$ . Dimensionless variables as follows.

$$\begin{aligned}\chi &= \frac{x}{r(0,0)} \\ \tau &= \frac{t}{t_{burntime}} \\ R &= \frac{r(x,t)}{r(0,0)} \\ \tilde{J}(x,t) &= \frac{\dot{m}_{port}}{\dot{m}_{ox}(0)} = \frac{\dot{m}_{ox}(t) + \dot{m}_f(x,t)}{\dot{m}_{ox}(0)} = \\ &= \frac{\dot{m}_{ox}(0) + \dot{m}_f(x,t)}{\dot{m}_{ox}(0)} + \left( \frac{\dot{m}_{ox}(t) - \dot{m}_{ox}(0)}{\dot{m}_{ox}(0)} \right) \\ J(x,t) &= \frac{\dot{m}_{ox}(0) + \dot{m}_f(x,t)}{\dot{m}_{ox}(0)} \\ \lambda(t) &= \frac{\dot{m}_{ox}(t) - \dot{m}_{ox}(0)}{\dot{m}_{ox}(0)}\end{aligned}\tag{11.19}$$

In dimensionless form, the coupled equations are

$$\frac{\partial R}{\partial \tau} = C_R \frac{1}{\chi^m} \left( \frac{J + \lambda}{\pi R^2} \right)^n\tag{11.20}$$

and

$$\frac{\partial J}{\partial \chi} = C_J \frac{(2\pi R)}{\chi^m} \left( \frac{J + \lambda}{\pi R^2} \right)^n \quad (11.21)$$

where

$$C_R = \frac{at_{burntime}\dot{m}_{ox}(0)^n}{r(0,0)^{2n+m+1}} \quad (11.22)$$

and

$$C_J = \frac{a\rho_f\dot{m}_{ox}(0)^{n-1}}{r(0,0)^{2n+m-2}}. \quad (11.23)$$

are dimensionless constants. The variable ranges are

$$0 < \chi < \frac{L_{port}}{r(0,0)} \quad (11.24)$$

$$0 < \tau < 1$$

where  $L_{port}$  is the port length.

Equations (11.20) and (11.21) can be integrated using a simple first order forward difference scheme.

Step 1 - Specify  $r(0,0)$ ,  $L_{port}$ ,  $t_{burntime}$ , and the regression rate constants,  $a$ ,  $n$ , and  $m$ . Calculate  $C_R$  and  $C_J$ . If the initial port radius is not constant along the port, specify  $R(\chi,0)$ . If the oxidizer mass flow rate varies with time, specify  $\lambda(\tau)$ .

Step 2 - Choose a grid of  $\chi$  and  $\tau$  coordinates.

$$\chi_i = (i/i_{max}) (L_{port}/r(0,0)), \quad i = 1, \dots, i_{max} \quad (11.25)$$

$$\tau_j = (j/j_{max}), \quad j = 1, \dots, j_{max}$$

Step 3 - Create tables defining the initial port geometry,  $R(\chi_i,0)$ ,  $i = 1, \dots, i_{max}$ , and oxidizer mass flow rate values,  $\lambda(\tau_j)$ ,  $j = 1, \dots, j_{max}$ .

Step 4 - Create tables defining the initial values of the radius and mass flow functions.

$$\begin{aligned}
R(\chi_i, \tau_j) &= R(\chi_i, 0), \quad i = 1, \dots, i_{\max}, \quad j = 1, \dots, j_{\max} \\
J(\chi_i, \tau_j) &= 1, \quad i = 1, \dots, i_{\max}, \quad j = 1, \dots, j_{\max}
\end{aligned}
\tag{11.26}$$

Step 5 - Update the  $R$  and  $J$  tables over the length of the port and for the length of the burn using the following first-order iterative scheme.

$$\begin{aligned}
R(\chi_i, \tau_{j+1}) &= R(\chi_i, \tau_j) + \Delta\tau \frac{C_R}{\chi_i^m} \left( \frac{J(\chi_i, \tau_j) + \lambda(\tau_j)}{\pi R(\chi_i, \tau_j)^2} \right)^n \\
J(\chi_{i+1}, \tau_j) &= J(\chi_i, \tau_j) + \Delta\chi \frac{C_J (2\pi R(\chi_i, \tau_j))}{\chi_i^m} \left( \frac{J(\chi_i, \tau_j) + \lambda(\tau_j)}{\pi R(\chi_i, \tau_j)^2} \right)^n
\end{aligned}
\tag{11.27}$$

$$i = 1, \dots, i_{\max} - 1$$

$$j = 1, \dots, j_{\max} - 1$$

where the differences in time and space are

$$\begin{aligned}
\Delta\tau &= 1/j_{\max} \\
\Delta\chi &= (1/i_{\max}) (L_{port}/r(0, 0)).
\end{aligned}
\tag{11.28}$$

The resulting tables of  $R(\chi_i, \tau_j)$  and  $J(\chi_i, \tau_j)$  can be used to generate all of the information needed to characterize the burn.

### 11.7.5 Example - Numerical solution of the coupled problem for a long burning, midsize motor as presented in reference [1].

Regression rate data in Figure 11.14 from the tests described above of a 10,000 Newton class hybrid rocket motor at NASA Ames led to the following exponents for Liquid Oxygen burning with Paraffin,  $n = 0.62$ ,  $m = 0.015$ . The multiplier was found to be  $a = 9.27 \times 10^{-5} m^{(2n+m+1)} kg^{-n} sec^{n-1} = 9.27 \times 10^{-5} m^{2.39} kg^{-0.62} sec^{-0.38}$ . Generally the motor ran for about 8 seconds during which time the port radius increased by a factor of a little less than 2. The port length is  $L_{port} = 1.143 m$ . Initially, the port radius is  $r(0, 0) = 0.0508 m$  and is constant along the port. The fuel density is  $\rho_f = 920.0 kg/m^3$ . In the numerical results shown in Figures 11.16 and 11.17, the burn is continued for up to 100 seconds.

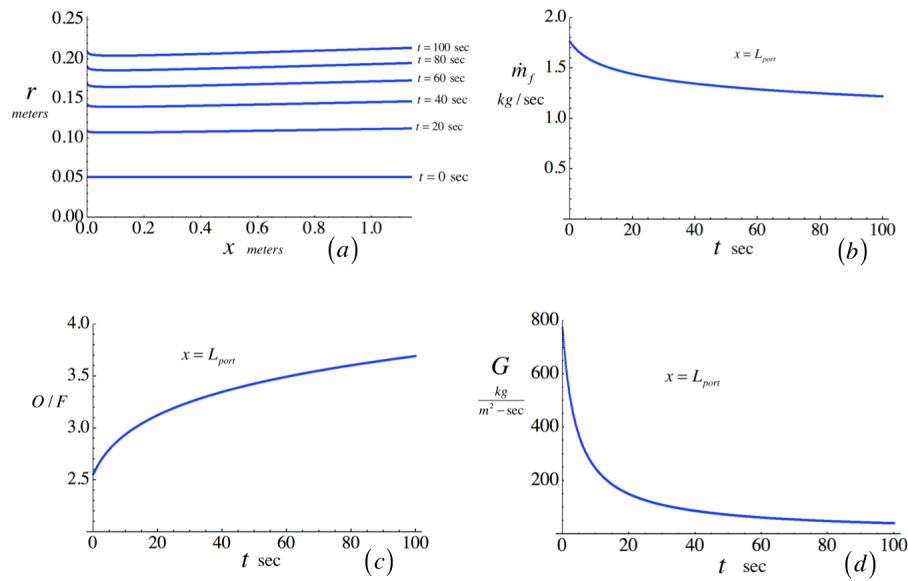


Figure 11.16: Port functions during a 100 sec burn; (a) Port radius as a function of  $x$  at several times during the burn; (b) Fuel mass flow as a function of time at the downstream end of the port; (c) Oxidizer to fuel ratio as a function of time at the downstream end of the port; (d) Mass flux as a function of time at the downstream end of the port.

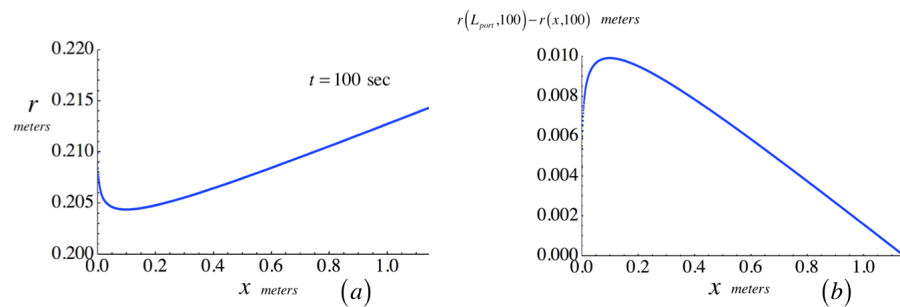


Figure 11.17: Port functions during a 100 sec burn; (a) Close-up of the port radius function of  $x$  at the end of the burn; (b) Unburned fuel sliver at the end of the burn.

The computations in Figures 11.16 and 11.17 were carried out on an  $i_{\max} = 2000$  by  $j_{\max} = 2000$  grid with uniform increments in the  $x$  and  $t$  directions. I used *Mathematica* for the computation which took 62 seconds on my 3.4 GHz Intel Core i7 imac. In the 2007 JPP paper, reference [1], a higher order scheme was used on a much coarser grid.

A couple of features in Figure 11.16 (a) should be mentioned. Due to the singularity in  $x$  in the denominator of the coupled equations, the radius and regression rate are infinite at  $x = 0$ . To avoid the singularity, the first numerical evaluation in  $x$  is at  $x = L_{port}/i_{\max}$ . The similarity solution described in the previous section can accurately resolve the solution near  $x = 0$ . There is a minimum in the port radius near the fore end of the port, the location of which depends on  $m$ . Beyond the minimum the port opens up slightly with the maximum radius occurring at the end of the port, a feature called "coning". Another important aspect of Figure 11.16 (a) is the slowing rate of increase in port radius with time as the burn progresses. This is reflected in Figure 11.16 (b) which depicts the decreasing rate of fuel generation as the port opens up, and in Figure 11.16 (c) which shows the corresponding increase in  $O/F$  ratio. For  $n > 0.5$  the decrease in mass flux depicted in Figure 11.16 (d) dominates the increase in port surface area leading to a decrease in the fuel mass flow rate with time. A consequence of the increase in port radius with  $x$  is that when the burn ends, there is a sliver of fuel that remains unburned. This is shown in Figure 11.17 (a) and (b). One way to alleviate this in practice is to fabricate the initial port with a slight decrease in radius with  $x$  and a computation of this case is included in reference [1]. The required amount of decrease depends on the planned burn time.

### 11.7.6 Sensitivity of the coupled space-time problem to small changes in $a$ , $n$ , and $m$ .

There is quite a bit of scatter in the data reported in the literature for the values of the regression rate parameters even for the same propellant combinations. It is of interest therefore to see how sensitive the regression rate is to small changes in the parameters  $a$ ,  $n$ , and  $m$ . Let the parameters be changed by small amounts.

$$\begin{aligned} a &\rightarrow aa' \\ n &\rightarrow n + n' \\ m &\rightarrow m + m' \end{aligned} \tag{11.29}$$

The regression rate equations become

$$\frac{\partial r(x, t)}{\partial t} = \frac{aa'}{x^{m+m'}} \left( \frac{\dot{m}_{port}(x, t) + \Delta \dot{m}_{ox}(t)}{\pi r^2} \right)^{n+n'} \quad (11.30)$$

$$\frac{\partial \dot{m}_{port}(x, t)}{\partial x} = \rho_f (2\pi r) \frac{(aa')}{x^{m+m'}} \left( \frac{\dot{m}_{port}(x, t) + \Delta \dot{m}_{ox}(t)}{\pi r^2} \right)^{n+n'}.$$

The ratio of the disturbed to undisturbed regression rate and mass flow rate is

$$\frac{\frac{\partial R}{\partial \tau}}{\frac{\partial R}{\partial \tau} \Big|_{(n', m')=(0,0)}} = \frac{\frac{\partial J}{\partial \chi}}{\frac{\partial J}{\partial \chi} \Big|_{(n', m')=(0,0)}} = \left( \frac{a' \pi^{n'}}{r(0,0)^{m'}} \left( \frac{\dot{m}_{ox}(0)}{\pi r(0,0)^2} \right)^{n'} \right) \frac{1}{(\chi)^{m'}} \left( \frac{J + \lambda}{\pi R^2} \right)^{n'} \quad (11.31)$$

The relative error in both rates is the same. Notice that  $a$  and  $a'$  do not have the same units and that  $a'$  is a number close to one.

$$[a] = \frac{L^{2n+m+1} T^{n-1}}{M^n} \quad (11.32)$$

$$[a'] = \frac{L^{2n'+m'} T^{n'}}{M^{n'}}$$

For small changes in  $n$  and  $m$ , and values of  $a'$  very close to one we can approximate Equation (11.31) as

$$\frac{\frac{\partial R}{\partial \tau}}{\frac{\partial R}{\partial \tau} \Big|_{(n', m')=(0,0)}} = \frac{\frac{\partial J}{\partial \chi}}{\frac{\partial J}{\partial \chi} \Big|_{(n', m')=(0,0)}} \cong$$

$$1 + n' \left\{ Ln \left( \frac{(a')^{1/n'} \pi}{r(0,0)^{m'/n'}} \left( \frac{\dot{m}_{ox}(0)}{\pi r(0,0)^2} \right) \right) + Ln \left( \frac{J + \lambda}{(\chi)^{m'/n'} \pi R^2} \right) \right\} \quad (11.33)$$

The first term in (11.33) in brackets is a fixed number and, to a good approximation, is the logarithm of  $\pi$  times the initial flux in the port, typically a number in the range 5 to 8. The second term in brackets is approximately the logarithm of the dimensionless flux in the port and depends on space and time. The dimensionless flux is generally less than one so this factor tends to be negative except near the port entrance. For  $m = 0$  the second factor is approximately  $Ln(1/\pi) = -1.14$ . In general, small changes in  $n$  change the rates

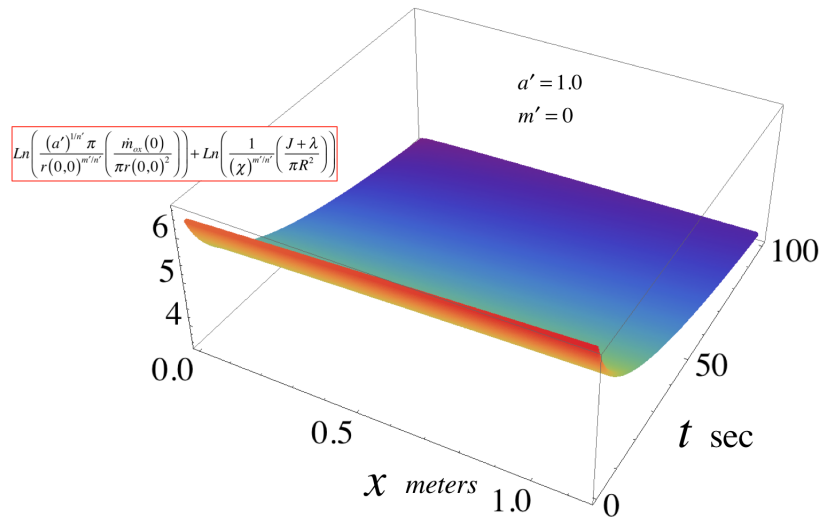


Figure 11.18: For the example considered in the previous section, sensitivity of the regression rate and mass flow rate to small changes in the exponent  $n$  for  $a' = 1$  and  $m' = 0$ .

substantially more than comparable changes in  $a$  or  $m$ . Figure 11.18 shows the sensitivity to small changes in  $n$  for the 100 second run considered in the last section.

#### References

- 1) Karabeyoglu, M. A., B. J. Cantwell, and G. Zilliac 2005. Development of Scalable Space-time Averaged Regression Rate Expressions for Hybrid Rockets, AIAA 2005-3544, 41st Joint Propulsion Conference, p.1-21 also Journal of Propulsion and Power, Vol. 23, No. 4 (2007), pp. 737-747. doi: 10.2514/1.19226
- 2) Cantwell, B. J., 2014 Similarity solution of fuel mass transfer, port mass flux coupling in hybrid propulsion, *Journal of Engineering Mathematics* (ISSN 0022 - 0833) (2014) 84:19-40. *J. Eng Math* (ISSN 1573 - 2703) DOI 10.1007/s10665-013-9624-y. This paper can also be found on my website.

## 11.8 Problems

**Problem 1** - The thrust versus time history of a hybrid rocket with a circular port is shown in Figure 11.19. The oxidizer mass flow rate is constant during the burn. The regression rate of the fuel surface follows a law of the form

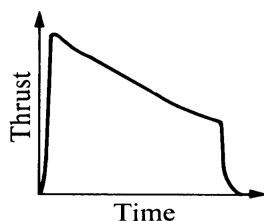


Figure 11.19: Typical thrust time history of a single circular port hybrid rocket.

$$\dot{r} = \alpha G^n \quad (11.34)$$

where the exponent  $n$  is in the range of 0.6 to 0.8 and  $G$  is the mass flux in the port. Briefly discuss why the thrust tends to decrease over the course of the burn. How would the thrust vary if the exponent was less than 0.5?

**Problem 2** - A research project at NASA Ames called Peregrine has the goal of launching a fairly large sounding rocket to an altitude of 100 km from NASA Wallops. The current design uses a paraffin -  $N_2O$  hybrid rocket motor that operates with a nozzle throat diameter of 10 cm and a nozzle exit diameter of 30 cm. The motor has a cylindrical port and the fuel grain is 143 cm long. At the beginning of the burn the  $N_2O$  mass flow is 24.0 kg/sec, and the port diameter is 23.3 cm. The diameter at the end of the port and the end of the burn is 38 cm. Assume that the mass flow rate of the  $N_2O$  is constant over the burn. The regression rate law in mks units is

$$\dot{r} = 14.84 \times 10^{-5} G^{0.5} \text{ m/sec} . \quad (11.35)$$

The paraffin density is 924.5 kg/m<sup>3</sup>. The chemical formula of the paraffin used is  $C_{32}H_{66}$  and the heat of formation is 698.52 kJ/mole.

- 1) Determine port diameter as a function of  $x$  at the end of the burn. How long is the burn? Assume the outer diameter of the fuel grain is constant and matches the port diameter at the end of the port at the end of the burn. What is the mass of unburned fuel?
- 2) Determine the mass flow rate and  $O/F$  ratio at the end of the port.
- 3) Determine the chamber pressure.
- 4) Plot the sea level thrust-time history of the motor and estimate the total delivered impulse (the integral of the thrust time curve). Use CEA to determine the specific impulse,  $C^*$  and the nozzle exit pressure.

**Problem 3** - A paraffin-oxygen hybrid rocket operates in a vacuum with a 10 *cm* diameter nozzle throat and a nozzle area ratio of 70. The motor has a cylindrical port 300 *cm* long. At the beginning of the burn the port is 20 *cm* in diameter and  $O/F = 2.3$ . The port diameter at the end of the burn is 60 *cm*. The regression rate law is

$$\dot{r} = 9.27 \times 10^{-5} G^{0.62} \text{ m/sec} . \quad (11.36)$$

The fuel density is 924.5 *kg/m*<sup>3</sup> and the combustion gas has  $\gamma = 1.15$  and average molecular weight equal to 30. Assume the oxidizer flow rate is constant and the combustion chamber temperature remains constant over the course of the burn. Approximate the specific impulse by a mean value of 360 *sec* over the course of the burn.

- 1) Estimate the chamber pressure at the beginning of the burn.
- 2) Plot the diameter of the port as a function of time.
- 3) Plot the thrust-time history of the burn and estimate the total delivered impulse (the integral of the thrust time curve).
- 4) Use Figure 11.4 to estimate the specific impulse at the end of the burn.

**Problem 4** - A hybrid rocket with an initial mass of  $m_{initial} = 900 \text{ kg}$  operates in space. The fuel is paraffin with a density 0.93 *gm/cm*<sup>3</sup> and the oxidizer is nitrous oxide. The oxidizer mass flow rate is held fixed at  $2.4 \times 10^4 \text{ gm/sec}$ . The motor has a 10 *cm* diameter nozzle throat, 30 *cm* diameter exit, and a cylindrical port 143 *cm* long. The initial port radius is 8.75 *cm*. At the end of the burn the port radius is 15.5 *cm*. The regression rate law is  $\dot{r} = 0.035 G_o^{0.6} \text{ cm/sec}$ . A calculation using CEA shows that  $c^* = 1.64 \times 10^5 \text{ cm/sec}$  where  $C^*$  is defined by  $\dot{m} = P_{t2} A^* / C^*$  and the effective nozzle exit velocity is  $C = 2.8 \times 10^5 \text{ cm/sec}$ .

- 1) When the fuel is all burned the oxidizer flow is turned off. Determine the time when this occurs.
- 2) Determine the total mass flow rate and motor thrust at the beginning and end of the burn.
- 3) Determine the chamber pressure at the beginning and end of the burn.
- 4) Determine the velocity change of the vehicle.